On the influence of the heart inflow boundary condition on local 3D flow patterns at the carotid artery

P.J. Blanco [a,*] M.R. Pivello [a] R.A. Feijóo [a] and S. A. Urquiza [b]

[a] *LNCC, Laboratório Nacional de Computação Científica, Av. Getúlio Vargas 333, Quitandinha, 25651–075, Petrópolis, RJ, Brasil, e–mail: pjblanco@lncc.br, pivello@lncc.br, feij@lncc.br*

[b] *Laboratorio de Bioingeniería, Universidad Nacional de Mar del Plata, Av. J.B. Justo 4302, 7600 Mar del Plata, Argentina, e–mail: santiagourquiza@fi.mdp.edu.ar*

Abstract

In this work we present a study on the influence of the heart inflow boundary condition on the blood flow pattern and on the arterial pulse conformation at the carotid artery. For this purpose, a 3D–1D coupled model for the simulation of the human cardiovascular system is used. The representation of the 1D arterial tree proposed by Avolio [1] is coupled with a 3D real model of the carotid artery acquired from a patient-specific MRI using image segmentation and reconstruction techniques. Different sets of heart ejection curves are applied as the inflow boundary condition, and the local behavior of the blood flow in the carotid bifurcation is then analysed. The main goal is to compare the flow pattern regarding recirculation regions by means of the computation of some well-known indicators, such as the OSI and WSS distributions.

Key words:
Blood Flow, Carotid Artery, Coupled Models, Inflow Boundary Condition, FEM.

* Corresponding author.
Email address: pjblanco@lncc.br (P.J. Blanco).

1 Introduction

The mathematical modeling of the Human Cardiovascular System has been recurrently used to better understand the phenomena involved in the conformation of the arterial pulse at different districts of the arterial system [1,7,8]. With this kind of information at hand full 3D models have also been incorporated in order to gain insight in the main characteristics of the local patterns of blood flow. Because of the complexity of the system, simulating the whole arterial system with full 3D models is still an unfeasible task. To overcome this issue, coupled 3D–1D models of the arterial system are employed [2,9]. In this kind of formulation, a simplified version of the Navier–Stokes equations in compliant vessels is used to account for the phenomena at the major arterial districts scale, whereas localized 3D models are used to study in detail the blood flow at regions of particular interest.

The 1D model of the arterial tree is represented not only by means of a given geometry and topology of the major arteries, but also by the effects of the peripheral beds and by the inflow boundary condition representing the ejection of the heart. In this way, the main goal of this work is to perform a study of the influence of the heart ejection curve on the characteristics of the hemodynamics at the carotid artery bifurcation, comparing quantities of interest defined on both 3D and 1D regions of the coupled model. Specifically, the influence of five different flow ejection curves on the flow rate and pressure curves (1D quantities), as well as local flow patterns at the carotid bifurcation and well-known indicators (3D quantities), will be studied.

2 The Model

The governing equations were derived based on a variational formulation for the coupling of kinematically incompatible models, in this case 3D-1D flow models in compliant vessels [2]. The associated Euler equations for a Newtonian fluid when coupling a 1D domain Ω_{1D} with a 3D region Ω_{3D} through a coupling interface Γ_c, and considering the ALE formulation over Ω_{3D}, are the following:

$$\rho A\frac{\partial \bar{u}}{\partial t}+\rho A\bar{u}\frac{\partial \bar{u}}{\partial z}=-A\frac{\partial \bar{p}}{\partial z}-8\pi\mu\bar{u}+f^z \qquad \text{in } \Omega_{1D}\times(0,T) \qquad (1)$$

$$\rho\left.\frac{\partial \mathbf{u}}{\partial t}\right|_{\mathbf{Y}}+\rho\nabla\mathbf{u}\left(\mathbf{u}-\mathbf{w}\right)=-\nabla p+\mu\Delta\mathbf{u}+\mathbf{f} \qquad \text{in } \Omega_{3D}\times(0,T) \qquad (2)$$

$$\frac{\partial A}{\partial t}+\frac{\partial\left(A\bar{u}\right)}{\partial z}=0 \qquad \text{in } \Omega_{1D}\times(0,T) \qquad (3)$$

$$\nabla \cdot \mathbf{u} = 0 \qquad \text{in } \Omega_{3D} \times (0,T) \tag{4}$$

$$(-p\mathbf{I} + 2\mu\boldsymbol{\varepsilon}(\mathbf{u}))\,\mathbf{n}_1 = -\bar{p}\mathbf{n}_1 \qquad \text{on } \Gamma_c \times (0,T) \tag{5}$$

$$A_c\bar{u} = \int_{\Gamma_c} \mathbf{u}\cdot\mathbf{n}_1 \; d\Gamma \qquad \text{on } \Gamma_c \times (0,T) \tag{6}$$

Where $\mathbf{n}_1$ is the unit outward normal to domain Ω_{1D} over the coupling interface Γ_c. In equations 1 and 3, which represent the 1D model, $\bar{u}$, $\bar{p}$ are the mean velocity and pressure values, ρ is the blood density, μ is the dynamic viscosity, A denotes the cross sectional area, $A\bar{u}$ is the flow rate and z is the axial coordinate. Equations 2 and 4 represent the 3D model, $\mathbf{u}$ is the blood velocity, $\mathbf{w}$ is the domain velocity of change consistent with the ALE framework and p is the blood pressure. Equation 5 stands for the continuity of the traction vector at Γ_c (the coupling interface between the 3D and 1D models), while expression 6 is the counterpart of the mass conservation.

The wall movement is modelled according to the independent ring model [5], and its equations are stated bellow:

$$\bar{p} = \bar{p}_0 + \frac{E\pi R_0 h_0}{A}\left(\sqrt{\frac{A}{A_0}} - 1\right) + \frac{k\pi R_0 h_0}{A}\frac{1}{2\sqrt{A_0 A}}\frac{\mathrm{d}A}{\mathrm{d}t} \qquad \text{in } \Omega_{1D} \times (0,T) \tag{7}$$

$$p = p_0 + \frac{Eh}{R_0^2}\zeta + \frac{kh}{R_0^2}\frac{\mathrm{d}\zeta}{\mathrm{d}t} \qquad \text{in } \Gamma_w \times (0,T) \tag{8}$$

The deformation of the domain Ω_{3D} is accounted for through a laplacian problem, as stated bellow:

$$\nabla^2\mathbf{d} = 0 \qquad \text{in} \qquad \Omega_{3D} \times (0,T) \tag{9}$$

Since it is a small amplitude movement, no remeshing is performed. Instead, equation 7 is used in order to extend the wall movement to the interior of Ω_{3D}, and $\mathbf{d}|_{\Gamma_w} = \zeta\mathbf{n}$ is the wall displacement, where ζ is the scalar field that denotes the displacement of the wall in the normal direction, given by $\mathbf{n}$, that is obtained from equation 8.

3 Numerical Approximation

In this section the numerical aspects of this work are briefly described. In this sense, details concerning the numerical techniques applied and the setting of the model regarding boundary conditions as well as the 3D geometry and the 1D arterial network topology are given.

The time discretization is performed by means of a single step finite diference

method corresponding to a classical θ scheme for both 1D and 3D parts. The spatial discretization is carried out through the Finite Element Method. Variables Q, A, $\bar{p}$ of the 1D model are discretized with $\mathbb{P}_1$ finite elements, while $\mathbf{u}$, p in the 3D model are discretized with $\mathbb{P}_1^B - \mathbb{P}_1$ finite elements. The index B stands for bubble functions for the velocity field according to the mini element formulation [3]. The domain displacement, $\mathbf{d}$, is also approximated with $\mathbb{P}_1$ finite elements, and the reference velocity $\mathbf{w}$ is computed from the displacement by a backward Euler difference scheme. For both 1D and 3D parts, stabilization terms must be included in order to avoid the non–physical oscillating solutions present in standard Galerkin approximations. For the 1D model these terms are incorporated along the characteristics lines and correspond to a Galerkin Least Squares formulation [9]. For the 3D model the stabilization terms correspond to the Streamline Upwind Petrov Galerkin technique with a suitable stabilization parameter [4]. In all cases, nonlinearities are treated with Picard iterations.

To perform the numerical tests, the 1D model of the arterial tree proposed by Avolio [1] was used. The geometry of the carotid artery was obtained via segmentation of magnetic ressonance images and then discretized with a finite element mesh. Figure 1 shows the topology of the arterial tree, as well as the location of the embedding of the 3D district within the 1D model. Five

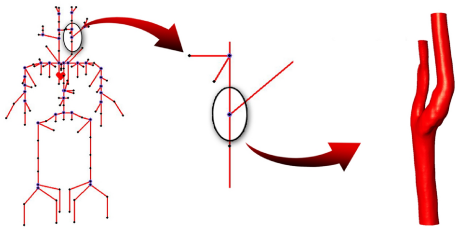

Fig. 1. Schematic coupling between 1D and 3D models.

different flow curves representing the cardiac ejection are tested as the inflow boundary condition for the 1D model, in order to assess their influence on the flow behavior on both 1D and 3D portions of the model. In all cases, the blood flow rate is 5 lt/min and the cardiac period is $T = 0.8$ sec. Figure 2 shows the flow rate versus time in a cardiac cycle, according to different works. From top to bottom, left to right: Avolio [1], Stergiopulos [7], Spencer [6], a modified version of the Spencer case(which decreases the systolic peak and increases systolic phase) and Stettler [8].

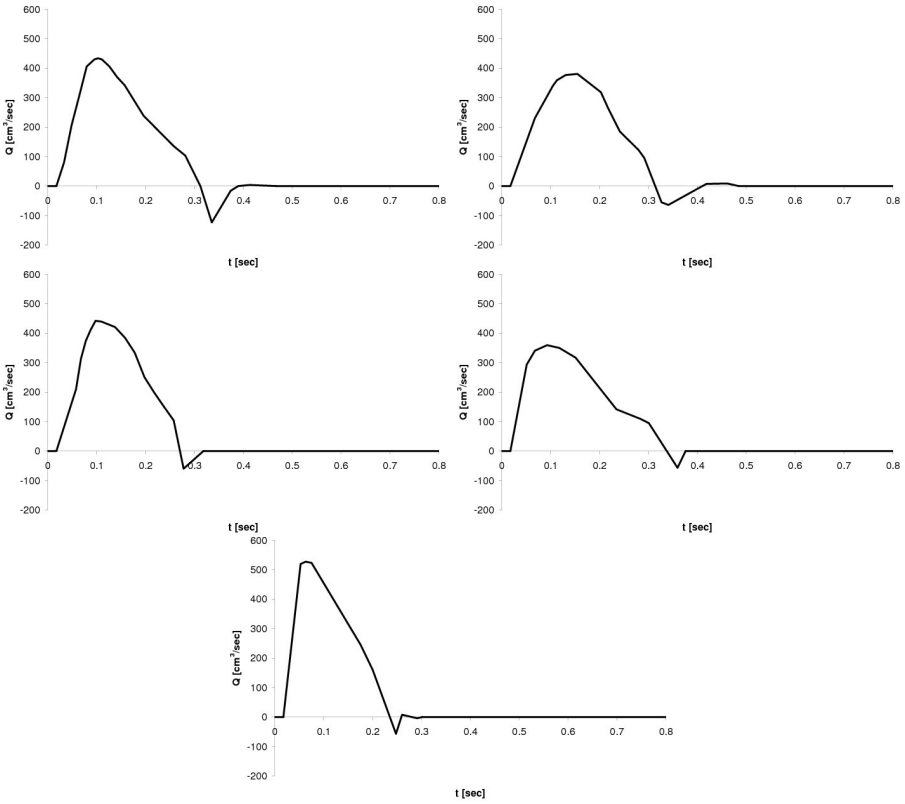

Fig. 2. Different heart ejection curves considered.

4 Results

The results corresponding to local blood flow patterns obtained after after using the five different heart ejection curves shown in figure 2 are presented here. For each case, one cardiac cycle was simulated and the blood was modelled as a non-newtonian fluid, following a Casson constitutive behavior.

Investigations on the 1D part of the model were carried out by analysing the time evolution of the flow rate and pressure at the interface between the 3D and 1D models at the common carotid for each ejection curve. As regards 3D flow patterns several comparisons are performed, including the computation of the OSI and WSS indicators.

Figures 3 and 4 show the flow rate and pressure curves for each cardiac ejection at the coupling interface between the 1D and 3D models at the common carotid. Results for the internal- and external- carotid coupling faces are very similar to this, and therefore are not shown here.

Comparing results from figures 3 and 4 with figure 2, it is clear that flow rate and pressure are very sensitive to the inflow boundary conditions in the 1D model. Indeed, the dissimilarities seem to be strongly related to the time

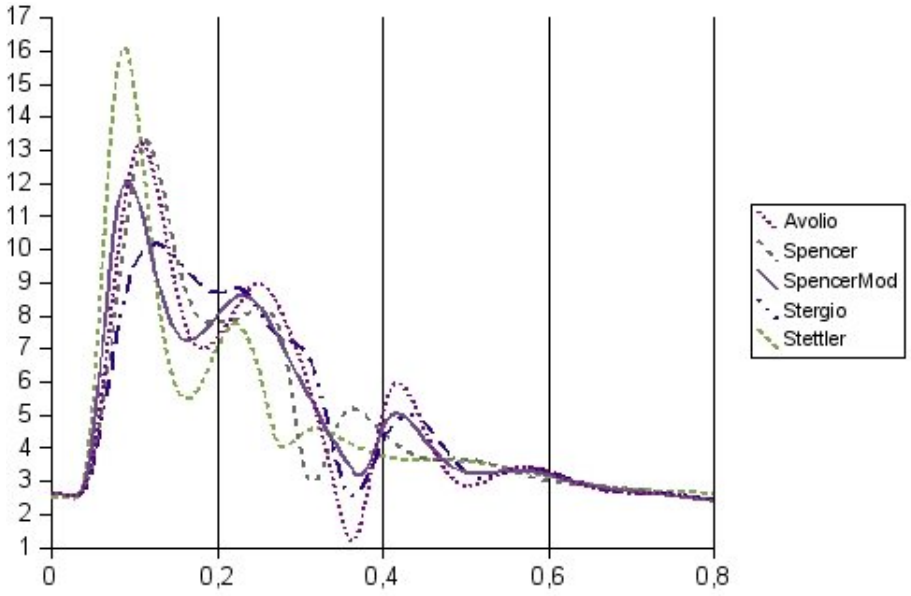

Fig. 3. Time evolution of the flow rate for the 5 heart ejection curves tested $\big(Q[cm^3/sec] \times t[sec]\big)$.

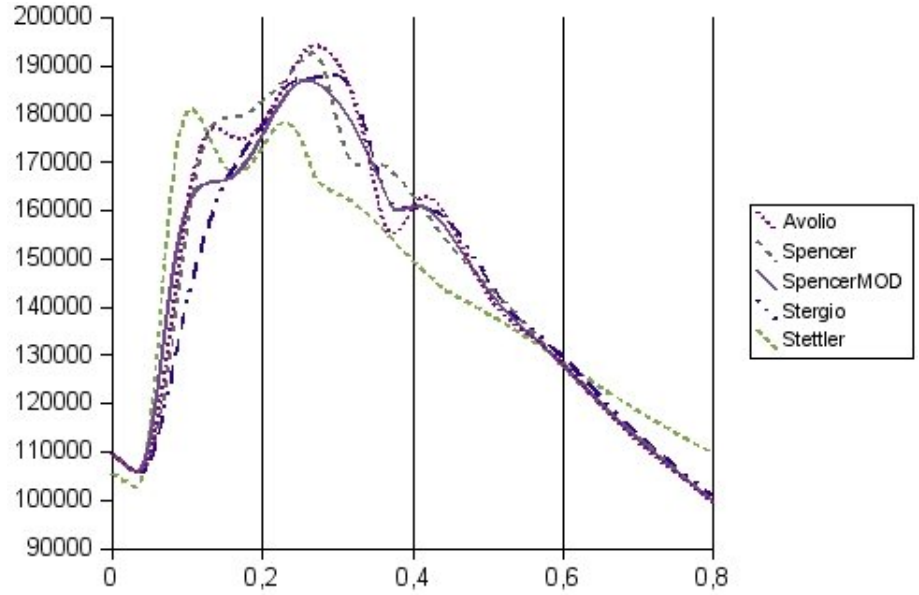

Fig. 4. Pressure time evolution for the 5 heart ejection curves tested $\big(P[dyn/cm^2] \times t[sec]\big)$.

derivative of the flow curve before reaching the systolic peak.

Figures 5 to 9 show the streamlines and velocity profiles at the carotid bifurcation at three different time instants for each heart ejection curve. The results were not taken at the same time instants instant because of the differences in the moments in which each projection curve reaches the relative extreme values. In each case, the first step is taken during the systolic phase after the

systolic peak, the second corresponds to the beginning of the diastolic phase, while the third one is taken at the last peak in the diastolic phase after the systolic peak.

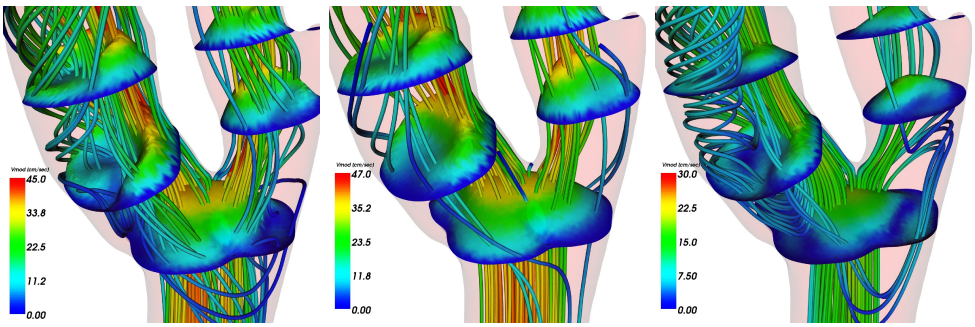

Fig. 5. Streamlines and velocity profiles at the carotid bifurcation for the Avolio cardiac ejection. From left to right: T=0.185s, T=0.250s and T=0.365s.

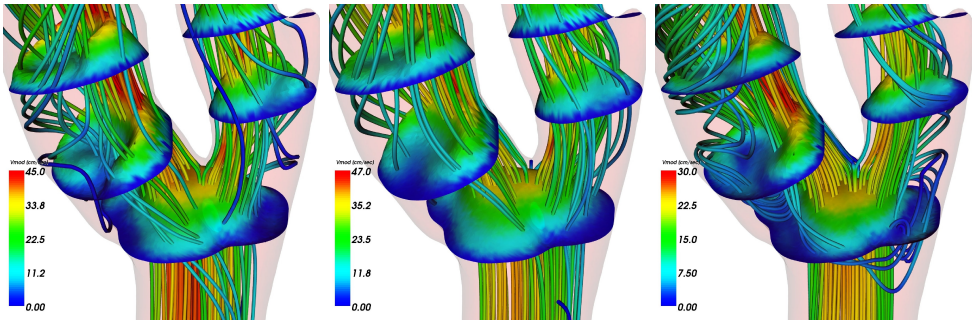

Fig. 6. Streamlines and velocity profiles at the carotid bifurcation for the Spencer cardiac ejection. From left to right: T=0.190s, T=0.255s and T=0.315s.

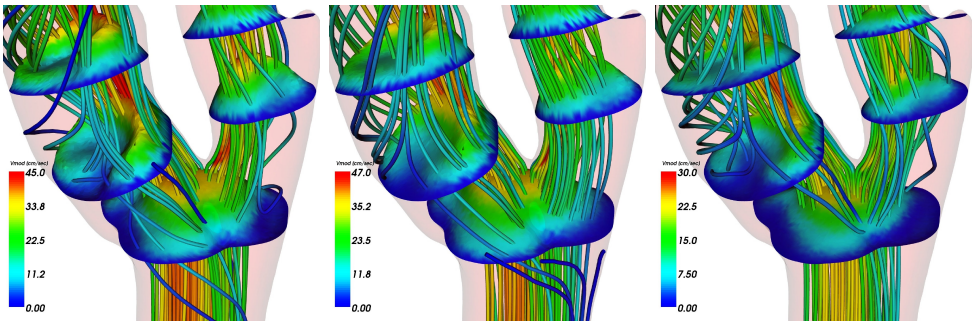

Fig. 7. Streamlines and velocity profiles at the carotid bifurcation for the Spencer-Mod cardiac ejection. From left to right: T=0.165s, T=0.230s and T=0.370s.

Figures 10 and 11 show the distribution of the OSI and WSS indicators respectively. In despite of the differences observed in the local patterns, no dissimilarities arise between the distribution of each one. This is a straightforward consequence of the low sensitivity of the flow patterns to the cardiac ejection. Therefore, we infer that when individuals have similar cardiac cycles and similar flow rates per cardiac cycle, the variability from one subject to another lies mainly in the differences in the geometry of the arterial district.

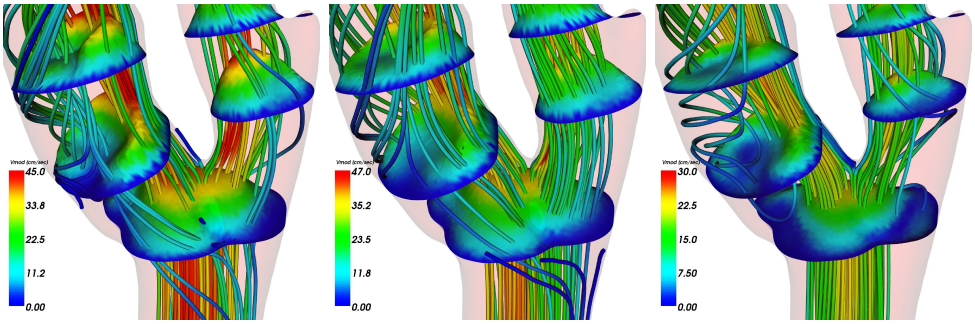

Fig. 8. Streamlines and velocity profiles at the carotid bifurcation for the Stergiopulos cardiac ejection. From left to right: T=0.205s, T=0.225s and T=0.365s.

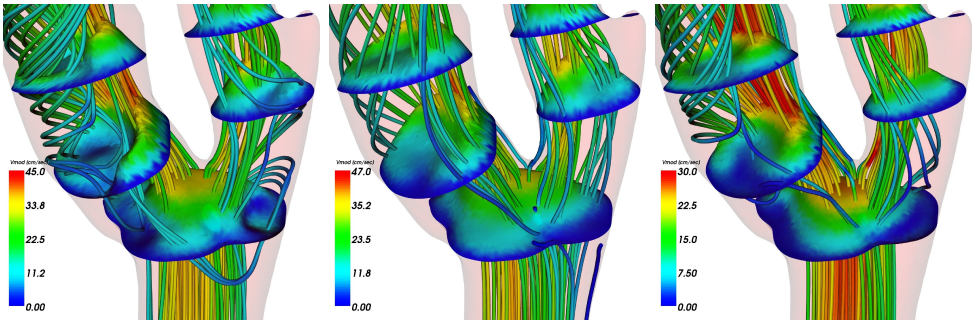

Fig. 9. Streamlines and velocity profiles at the carotid bifurcation for the Stettler cardiac ejection. From left to right: T=0.165s, T=0.225s and T=0.280s.

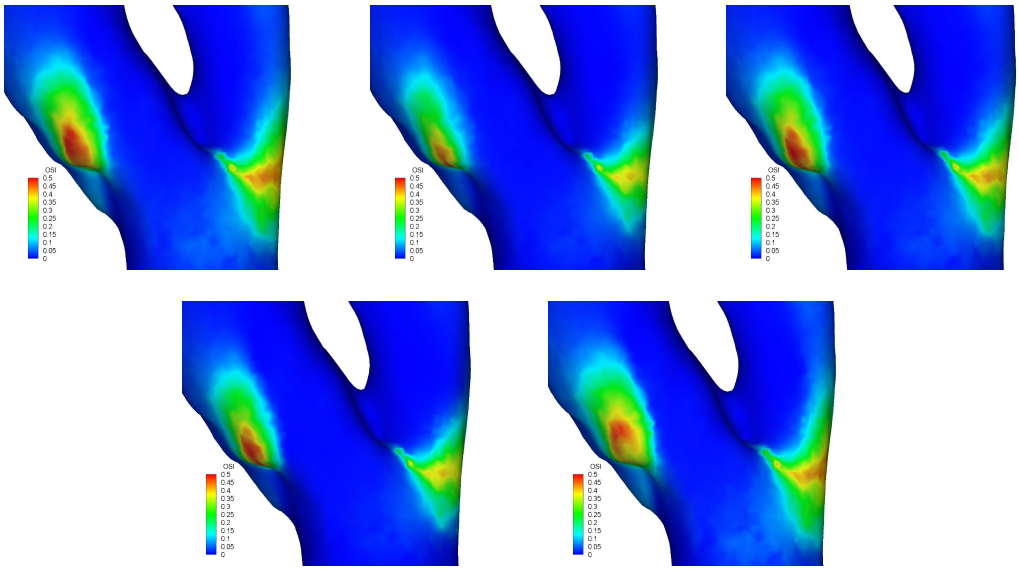

Fig. 10. OSI distribution for the different cardiac ejection curves. From top to bottom, left to right: Avolio, Stergiopulos, Spencer, SpencerMod and Stettler.

5 Conclusions

A numerical study was performed to assess the influence of the heart ejection curve on both local flow patterns and global flow and pressure curves by using

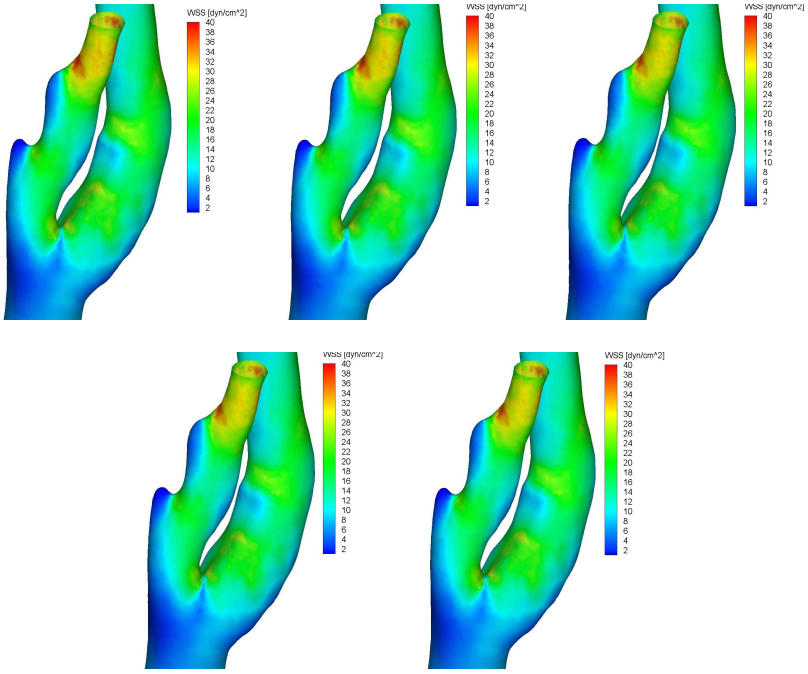

Fig. 11. WSS distribution for the different cardiac ejection curves. From top to bottom, left to right: Avolio, Stergiopulos, Spencer, SpencerMod and Stettler.

a 3D-1D coupled model. Five different curves were tested, all of them having the same period and average flow rate per cardiac period. The response of the 1D model to the different inflow curves varied considerably, what is in agree with respect to the variability encountered between different subjects. On the other hand, local flow patterns were nearly insensitive to the alteration of the inflow boundary condition. As a result, the indicators computed from the flow structure did not present significant differences, evidencing the lack of sensitivity of the flow structure to the morphology of the cardiac ejection under the considerations taken in this work. Therefore, we conclude that, while the phenomena occurring at the level of the arterial network is highly dependant upon the cardiac ejection, local phenomena is mainly governed by the geometrical characteristics of the vascular district, always keeping in mind the invariance of the cardiac period and of the average flow rate.

References

[1] A.P. Avolio. Multi–branched model of the human arterial system. *Med. Biol. Engrg. Comp.*, 18:709–718, 1980.

[2] P.J. Blanco, R.A. Feijóo, and S.A. Urquiza. A consistent variational approach for coupling 3D–1D models. Accepted for publishing in Comp. Meth. Appl. Mech. Engrg., 2007.

[3] D.N.Arnold, F.Brezzi, and M.Fortin. A stable finite element for the stokes equations. *Calcolo*, (21), 1984.

[4] T.J.R. Hughes, L.P. Franca, and M. Mallet. A new finite element formulation for computational fluid dynamics: Vi. convergence analisys of the generalized supg formulation for linear time-dependent multimensinal advective-diffusive systems. *Comp. Meth. Appl. Mech. Engrg.*, (63):97–112, 1987.

[5] Y. Kivity and R. Collins. Nonlinear fluid–shell interactions: application to blood flow in large arteries. *Int. Sym. Discrete Meth. Engrg.*, pages 476–488, 1974.

[6] M.P. Spencer and A.B. Deninson. The square–wave electro–magnetic flowmeter. theory of operation and design of magnetic probes for clinical and experimental applications. *I.R.E. Trans. Med. Elect.*, 6:220–228, 1959.

[7] N. Stergiopulos, D.F. Young, and T.R. Rogge. Computer simulation of arterial flow with applications to arterial and aortic stenoses. *JB*, 25:1477–1488, 1992.

[8] J.C. Stettler, P. Niederer, and M. Anliker. Theoretical analysis of arterial hemodynamics including the influence of bifurcations, part I. *Ann. Biomed. Engrg.*, 9:145–164, 1981.

[9] S.A. Urquiza, P.J. Blanco, M.J. Vénere, and R.A. Feijóo. Multidimensional modeling for the carotid blood flow. *Comput. Meth. Appl. Mech. Engrg.*, 195:4002–4017, 2006.